Journal of Zhejiang University-SCIENCE B 2025 26(12):1172-1191
www.jzus.zju.edu.cn; www.springer.com/journal/11585
E-mail: jzus_b@zju.edu.cn

Research Article
https://doi.org/10.1631/jzus.B2500254

Check for updates

Single-cell RNA-sequencing-guided reactive oxygen species-scavenging hydrogel design for regeneration of osteoporotic bone

Wei HU[1*], Tianyi FEI[2*], Zhichao LIU[2], Yude DING[1], Mengfei YU[2], Fan YANG[1✉], Feiya ZHAO[1✉]

[1]*Center for Plastic & Reconstructive Surgery, Department of Stomatology, Zhejiang Provincial People's Hospital, Affiliated People's Hospital, Hangzhou Medical College, Hangzhou 310014, China*
[2]*Stomatology Hospital, School of Stomatology, Zhejiang University School of Medicine, Zhejiang Provincial Clinical Research Center for Oral Diseases, Zhejiang Key Laboratory of Oral Biomedical, Engineering Research Center of Oral Biomaterials and Devices of Zhejiang Province, Hangzhou 310000, China*

Abstract: The pathological microenvironment of osteoporosis poses a substantial clinical challenge for bone defect regeneration. Through single-cell RNA-sequencing (scRNA-seq) analysis, we identified a reactive oxygen species (ROS)-overloading osteoblast subpopulation as a critical pathological feature of osteoporotic niches. Guided by scRNA-seq analysis, we engineered a microenvironment-adaptive hydrogel system through precise integration of antioxidant curcumin-encapsulated zeolitic imidazolate framework-8 nanoparticles (CCM@ZIF-8 NPs) within photo-crosslinkable alginate methacrylate (AlgMA) hydrogel (AlgMA/CCM@ZIF-8). This engineered design exhibited dual functions: effectively scavenging ROS in bone marrow-derived mesenchymal stem cells (BMSCs) while simultaneously suppressing osteoclast differentiation. The osteo-regenerative superiority of the AlgMA/CCM@ZIF-8 nanocomposite hydrogel was conclusively demonstrated in bone defect models of osteoporotic mice. This scRNA-seq-informed engineering strategy offers a promising approach for developing pathophysiology-adapted biomaterials to promote regenerative repair in osteoporotic bone defects.

Key words: Osteoporosis; Single-cell RNA-sequencing (scRNA-seq); Reactive oxygen species (ROS); Curcumin (CCM); Bone regeneration

1 Introduction

Osteoporosis is a prevalent systemic skeletal disorder characterized by progressive bone loss, microarchitectural deterioration, increased fragility, and heightened susceptibility to fractures (Chen et al., 2024). With a global prevalence exceeding 200 million cases (Wu et al., 2020), osteoporosis is responsible for approximately 8.9 million fragility fractures annually (The Lancet Diabetes & Endocrinology, 2021), imposing a substantial socioeconomic burden.

Emerging evidence has highlighted the pivotal roles of skeletal aging and chronic inflammation in the pathogenesis (Yu and Wang, 2016). Large-scale human epidemiological cohort studies have recently shown a significant correlation between elevated levels of systemic inflammatory markers and increased risk of osteoporotic fractures (Barbour et al., 2014). Extensive research has established that inflammation and excessive reactive oxygen species (ROS) generation, along with the resultant oxidative stress, play a pivotal role in modulating bone healing processes (de Oliveira et al., 2020; Sheng et al., 2023; Chen W et al., 2025). However, the precise alterations within the bone marrow microenvironment during osteoporosis progression remain poorly understood, and the production and pathophysiological involvement of ROS in different cell populations remain key knowledge gaps in the field (Iantomasi et al., 2023).

The lack of a precise understanding of the osteoporotic microenvironment has led to the current

✉ Feiya ZHAO, zhaofeiya@hmc.edu.cn
Fan YANG, yangfan@hmc.edu.cn
* The two authors contributed equally to this work
Feiya ZHAO, https://orcid.org/0000-0001-7159-1934
Fan YANG, https://orcid.org/0000-0002-1308-4827
Wei HU, https://orcid.org/0009-0007-2485-2303

Received May 14, 2025; Revision accepted Sept. 21, 2025; Crosschecked Dec. 4, 2025

commonly used osteoporosis drugs, such as bisphosphonates, denosumab, and parathyroid hormone (Zhang et al., 2023), with limited specificity. Consequently, their application is constrained by systemic side effects, the need for high dosages, and reduced local effectiveness (Guan et al., 2024). Moreover, bisphosphonates and denosumab are tightly correlated with medication-related osteonecrosis of the jaw (Cho et al., 2024). Therefore, elucidating the precise characteristics of the osteoporotic cellular microenvironment, including its oxidative stress status, and developing a localized drug delivery system based on these insights hold critical significance for the treatment of osteoporotic bone defects.

Curcumin (CCM), a polyphenolic compound derived from the rhizome of turmeric, has attracted significant attention for its multifaceted therapeutic potential, particularly due to its potent antioxidant, anti-inflammatory, and immunomodulatory properties (Yang XM et al., 2023; Amaroli et al., 2024; Wang JJ et al., 2024; Zhang JY et al., 2024). Mechanistically, CCM directly scavenges ROS, including superoxide anion radicals generated by the xanthine oxidase system and hydroxyl radicals produced during Fenton reactions (Wang et al., 2025). CCM enhances the expression of catalase (CAT) (Li Y et al., 2024) and nuclear factor erythroid 2-related factor 2 (NRF2) (Li et al., 2023; Li Y et al., 2024), thereby effectively scavenging intracellular ROS. Despite these promising therapeutic properties, the clinical translation of CCM is significantly constrained by its poor pharmacokinetic profile, characterized by limited aqueous solubility, low absorption, and diminished effectiveness in vivo (Inchingolo et al., 2024). Biomaterials functionalized with metal-organic frameworks (MOFs) represent a class of advanced materials characterized by high specific surface area, high porosity, and controllable degradability (Zhao et al., 2023; Li SW et al., 2024). Zeolitic imidazolate framework-8 (ZIF-8) exhibits suitability as a carrier for CCM owing to its distinctive structural and physicochemical characteristics (Teimouri et al., 2024; Yan et al., 2024). ZIF-8 is synthesized through the coordination-driven self-assembly of zinc ions (Zn^{2+}) with 2-methylimidazole (2-MIM) organic linkers, forming a hybrid framework that combines the advantageous characteristics of both MOFs and zeolite materials (Zhang X et al., 2024). This unique structure endows ZIF-8 with high porosity, large surface area, and abundant unsaturated metal sites, which collectively enhance its loading capacity for hydrophobic therapeutic drugs. Alginate methacrylate (AlgMA) is a versatile biomaterial with extensive applications in drug delivery, tissue engineering, bioprinting, and wound healing (Tomić et al., 2023). As a photo-crosslinkable derivative of natural alginate, AlgMA retains excellent biocompatibility while gaining spatiotemporal control over gelation through light-initiated polymerization. Its inherent porous structure facilitates drug loading and cell infiltration (Zhang FS et al., 2024). It has been engineered to address critical challenges in massive bone defect regeneration (Huang et al., 2025).

Single-cell RNA-sequencing (scRNA-seq) technology, with its high-throughput capacity and single-cell resolution, enables the analysis of transcriptomic expression profiles at the single-cell level across diverse cell subpopulations (Lin et al., 2024). This approach has the potential to fully elucidate the heterogeneity and dynamics of various cell types, as well as intercellular interactions within the osteoporotic microenvironment. In this study, we used scRNA-seq to systematically characterize the pathological landscape of human osteoporotic bone. Our analysis revealed two critical findings: (1) neutrophils exhibit excessive ROS production during bone remodeling in osteoporotic conditions; (2) osteoblasts show heightened sensitivity to ROS-mediated stress (Fig. 1). Building on these mechanistic insights, we engineered a microenvironment-responsive hydrogel system (AlgMA/CCM@ZIF-8) through rational integration of CCM-loaded ZIF-8 nanoparticles (NPs) into a photo-crosslinkable alginate matrix. This innovative design simultaneously addresses multiple pathological features: (1) effectively scavenging excess ROS in osteoblasts; (2) suppressing osteoclast differentiation; and (3) rebalancing bone remodeling dynamics. Remarkably, this targeted intervention not only promoted functional bone regeneration in osteoporotic defects but also restored bone microarchitecture to near-physiological levels.

2 Materials and methods

2.1 scRNA-seq analysis

Publicly available scRNA-seq data from four osteoporotic femoral head samples (Gene Expression Omnibus (GEO) accession: GSE169396) were processed and analyzed (Qiu et al., 2021). Raw count matrices were imported into Seurat (version 4.3.0, implemented in R) for quality control (QC), retaining cells with >10

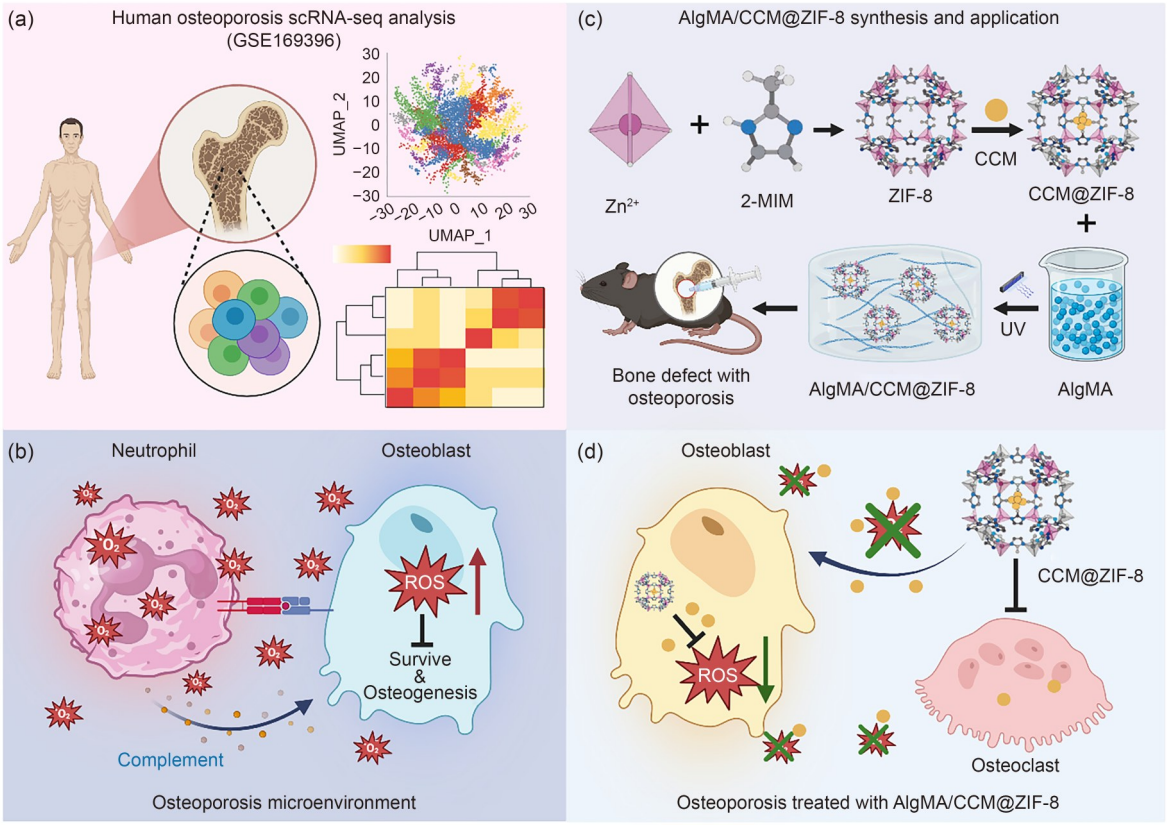

Fig. 1 Schematic illustration of single-cell RNA-sequencing (scRNA-seq)-guided reactive oxygen species (ROS) scavenging via alginate methacrylate/curcumin-encapsulated zeolitic imidazolate framework-8 (AlgMA/CCM@ZIF-8) nanocomposite hydrogel for bone defect regeneration in osteoporosis. (a) scRNA-seq analysis characterizes the cellular composition and microenvironment in human osteoporotic femoral samples. (b) scRNA-seq analysis reveals excessive ROS production by neutrophils under osteoporotic conditions, triggering hyper-oxidative stress in osteoblasts. (c) Synthesis and biomedical application of AlgMA/CCM@ZIF-8 nanocomposite hydrogel. (d) The AlgMA/CCM@ZIF-8 nanocomposite hydrogel promotes bone regeneration by remodeling the osteoporotic microenvironment, via scavenging ROS in osteoblasts and suppressing osteoclast differentiation. 2-MIM: 2-methylimidazole. Created with BioRender.com.

and <8000 detected genes, and a mitochondrial gene content of <20%. After QC, data were normalized using the "LogNormalize" method, and variable features were identified for principal component analysis (PCA). Dimensionality reduction was performed using Uniform Manifold Approximation and Projection (UMAP) with the top 30 principal components.

Cell clusters were annotated based on canonical marker genes. Differential gene expression analysis among clusters was conducted with the Wilcoxon rank-sum test (adjusted P-value<0.05, $|\log_2(\text{fold change})|>0.25$). Marker genes of each cluster were visualized in volcano plots using the scRNAtoolVis (version 0.0.7) package.

To assess ROS-related pathways, gene set scoring was performed using AddModuleScore with GOBP_REACTIVE_OXYGEN_SPECIES_BIOSYNTHETIC_PROCESS (https://www.gsea-msigdb.org/gsea/msigdb/human/geneset/GOBP_REACTIVE_OXYGEN_SPECIES_BIOSYNTHETIC_PROCESS) and GOBP_RESPONSE_TO_REACTIVE_OXYGEN_SPECIES (https://www.gsea-msigdb.org/gsea/msigdb/human/geneset/GOBP_RESPONSE_TO_REACTIVE_OXYGEN_SPECIES). Scores were compared across cell clusters and visualized as violin plots. All analyses were implemented in R (v4.2.3) with the tidyverse (version 1.3.2), Seurat (version 4.3.0), and clusterProfiler (version 4.4.4) packages.

To uncover potential ligand receptor interactions between different cell clusters, CellChat (version 1.6.1, R) was carried out. The heatmap, netVisual_circle, and netVisual_bubble functions were used to visualize the network and identify the senders and receivers involved in cell–cell communication.

2.2 Syntheses of ZIF-8 and CCM@ZIF-8 NPs

2.2.1 ZIF-8 NP synthesis process

ZIF-8 NPs were synthesized using a previously reported method with some modifications (Au-Duong and Lee, 2017). Firstly, 2.5 mmol (0.7333 g) of zinc nitrate hexahydrate ($Zn(NO_3)_2 \cdot 6H_2O$; Aladdin, China) was dissolved in 20 mL of methanol (high-performance liquid chromatography (HPLC) grade; Aladdin), while 40 mmol (3.2446 g) of 2-MIM (Aladdin) was separately dissolved in 80 mL of methanol. The two methanolic solutions were then combined and stirred for 4 h at room temperature, followed by incubation at 50 ℃ for 1 h. The mixture was subsequently centrifuged at 10 000 r/min for 10 min. The obtained precipitate was washed with methanol and centrifuged again under the same conditions. Finally, the product was dried overnight at 60 ℃ in a convection oven.

2.2.2 CCM@ZIF-8 NP synthesis process

CCM was incorporated into the ZIF-8 NPs using the following procedure: Firstly, 0.05 mg of CCM (MCE, USA) was co-dissolved with 2.5 mmol (0.7333 g) of $Zn(NO_3)_2 \cdot 6H_2O$ in 20 mL of methanol. The subsequent synthesis steps, including solution combination, stirring, incubation, centrifugation, washing, and drying, were identical to those described for the preparation of ZIF-8 NPs.

2.3 Surface characterization of ZIF-8 NPs and CCM@ZIF-8 NPs

2.3.1 Scanning electron microscopy and transmission electron microscopy analyses

Morphological assessment was conducted to evaluate variation in the appearance and sizes of the two nanoparticles using scanning electron microscopy (SEM) and transmission electron microscopy (TEM). Samples were coated with a 15-nm-thick layer of gold using a fully automated high vacuum coater, Q150T PLUS™ (Quorum Technologies, Wallruf, UK), for 70 s. Initial SEM images were acquired using an SM300™ scanning electron microscope (Topcon, Singapore). Subsequent SEM images were captured using a GeminiSEM 300™ scanning electron microscope (Zeiss, Germany). TEM images were acquired using an HT7700 EXALENS™ microscope (Hitachi, Japan).

2.3.2 Fourier-transform infrared analysis

Fourier-transform infrared (FTIR) spectroscopy was conducted to characterize the chemical composition of the samples using a Vertex 70™ Fourier-transform infrared spectrophotometer (Bruker, Germany). Spectra were acquired at room temperature over the wavenumber range of 4000–400 cm^{-1}.

2.3.3 In vitro CCM release from CCM@ZIF-8 NPs and AlgMA/CCM@ZIF-8

For the bare nanocomposite system, 5.0 mg of CCM@ZIF-8 NPs was homogenously suspended in 20 mL of 0.01 mol/L phosphate-buffered saline (PBS) supplemented with 0.5% (5 g/L) Tween 20 to ensure sink condition maintenance. Parallel evaluation of the alginate-encapsulated formulation was performed using a dialysis membrane technique (molecular weight cutoff (MWCO) 3.5 kDa). Specifically, 5.0 mg of CCM@ZIF-8 NPs was uniformly incorporated into 2.0 mL of 5% (50 g/L) AlgMA hydrogel precursor solution, followed by ultraviolet (UV)-induced photocrosslinking (λ=405 nm) for 15 s to form the AlgMA/CCM@ZIF-8 nanocomposite hydrogel. Both release studies were conducted under two different pH conditions: (1) pH=7.4, representing a healthy bone marrow microenvironment; (2) pH=5.5, simulating osteoporotic pathological conditions. All release experiments were performed under controlled conditions (37 ℃, 150 r/min orbital agitation) with temporal sampling at defined intervals (0–12 h: hourly; 24–80 h: terminal endpoints). For the direct suspension system, aliquots were centrifuged (10 000*g*, 5 min, 4 ℃; rotor radius 8.6 cm), while the dialysis system used medium replacement to maintain concentration gradients. CCM release was quantified by spectrophotometric analysis (λ=425 nm) using a standard curve.

2.4 In vitro experiments

2.4.1 Cell preparation and cytotoxicity assay

Bone marrow-derived mesenchymal stem cells (BMSCs) were initially extracted from the tibia and femur of 6-week-old C57BL/6J mice. BMSCs were cultivated in 25 cm^2 flasks (Corning, USA) using minimum essential medium α (α-MEM; Cienry, China) supplemented with 10% (volume fraction) fetal bovine serum (FBS; Gibco, USA) and 1% (volume fraction) penicillin-streptomycin, incubated in a humidified

atmosphere at 37 °C with 5% (volume fraction) CO_2, with the culture medium replaced every 2 d to maintain optimal growth conditions. Cells were passaged before reaching about 90% surface coverage. For subsequent biological studies, passage 2 and passage 3 BMSCs were used to ensure consistent and reliable experimental results.

To determine the appropriate dose of CCM@ZIF-8 NPs for enhancing cell proliferation, a cell counting kit-8 (CCK-8) assay (GlpBio, USA) was conducted using a cell density of 1×10^4 cells/mL. The results were obtained after 24 and 48 h of incubation with various concentrations of CCM@ZIF-8 NPs to identify the optimal concentration that promotes cell proliferation without inducing cytotoxicity. To further assess the toxicity of the selected concentration on both BMSCs and mouse mononuclear macrophage cells (RAW264.7) (ICell, Shanghai, China; m047), live/dead cell staining was performed using calcein acetoxymethyl ester (calcein AM), which fluoresces green in live cells and propidium iodide, which stains dead cells red (MKBio, China). Cells were seeded at a density of 1×10^4 cells/mL and stained after coculturing with the selected concentration of ZIF-8 and CCM@ZIF-8 NPs for 24 h. Subsequently, the cells were examined using an EVOS M5000™ fluorescence microscope (Invitrogen, USA).

2.4.2 Intracellular uptake of CCM@ZIF-8 NPs

To prove that CCM@ZIF-8 NPs can be internalized, BMSCs and RAW264.7 were co-cultured with ZIF-8 and CCM@ZIF-8 NPs (both 20 μg/mL), respectively, for 24 h in vitro. Subsequently, the cells were examined using laser confocal microscope (Zeiss) to determine the presence of spontaneous green fluorescence of CCM, indicating the successful internalization of CCM@ZIF-8 NPs into the cells.

2.4.3 Tartrate-resistant acid phosphatase staining for osteoclast formation

RAW264.7 cells were cultivated in osteoclastic differentiation medium (PH Biotechnology, Wuxi, China; CTCC-Y005) at a density of 2×10^5 cells/mL for 7 d in three groups: control, ZIF-8 NPs (20 μg/mL), and CCM@ZIF-8 NPs (20 μg/mL). Subsequently, cells were rinsed with PBS, stained using the tartrate-resistant acid phosphatase (TRAP) staining kit (Amizona, China), and documented using a multifunctional fluorescent imaging equipment BZ-X800LE (Keens, Japan).

2.4.4 RT-PCR assay

Real-time polymerase chain reaction (RT-PCR) was conducted to evaluate the expression levels of osteoclast-related genes. RAW264.7 cells were cultivated in osteoclastic differentiation medium at a density of 2×10^5 cells/mL for 7 d in three groups: control, ZIF-8 NPs (20 μg/mL), and CCM@ZIF-8 NPs (20 μg/mL). After incubation, cells were rinsed twice with PBS, and total RNA was extracted. The RNA was then reverse transcribed into complementary DNA (cDNA) using the PrimeScript RT reagent kit (TaKaRa, Japan). Gene expression levels of *TRAP*, cathepsin K (*Ctsk*), and cellular proto-oncogene *fos* (*c-Fos*) were analyzed using SYBR Premix Ex Taq II (TaKaRa) with the specific primers listed in Table 1. The expression levels of these target genes were normalized to glyceraldehyde-3-phosphate dehydrogenase (*GAPDH*) as an internal control.

Table 1 Primer sequences of the genes involved in this study

Primer	Species	Sequence (5'→3')
TRAP-F	Mice	CTGGAGTGCACGATGCCAGCGACA
TRAP-R	Mice	TCCGTGCTCGGCGATGGACCAGA
Ctsk-F	Mice	CTTCCAATACGTGCAGCAGA
Ctsk-R	Mice	TCTTCAGGGCTTTCTCGTTC
c-Fos-F	Mice	CCAGTCAAGAGCATCAGCAA
c-Fos-R	Mice	AAGTAGTGCAGCCCGGAGTA
GAPDH-F	Mice	ACCCAGAAGACTGTGGATGG
GAPDH-R	Mice	CACATTGGGGGTAGGAACAC

F: forward; R: reverse.

2.4.5 Western blot analysis

BMSCs were seeded on 6-well plates (1×10^5 cells per well) with 500 μmol/L H_2O_2 for 24 h to establish an oxidative stress model. Experimental groups were treated with ZIF-8 or CCM@ZIF-8 NPs (co-incubated with H_2O_2-challenged BMSCs for 24 h). Then, the lysates of BMSCs were collected, and protein extraction was conducted. The protein concentration was determined by the bicinchoninic acid (BCA) method according to the instructions of the BCA kit (Beyotime, China). The resulting proteins were analyzed by gel electrophoresis and transferred to nitrocellulose membranes (Beyotime). The membranes were sealed for 15 min using QuickBlock block buffer (Beyotime) and incubated with primary antibody, including NRF2 polyclonal antibody (Proteintech, China; 33123-1-AP) and GAPDH

antibody (Abcam, UK; ab8245) overnight at 4 °C. The membranes were then incubated with horseradish peroxidase (HRP)-conjugated goat anti-rabbit immunoglobulin G (IgG; Huabio, China; HA1001) for 1 h at room temperature. Protein bands were visualized using an enhanced chemiluminescence (ECL) kit (Beyotime). Then the chemiluminescent signals were detected using ChemiDocTM Touch (Bio-Rad, USA), and the band intensities were quantified using ImageJ software (National Institutes of Health, Bethesda, MD, USA).

2.4.6 ROS level measurement

To validate the antioxidant capacity of nanoparticles on BMSCs, intracellular ROS levels were assessed through dual-modality detection (confocal microscopy and flow cytometry). BMSCs were primed with 500 μmol/L H_2O_2 for 24 h to establish an oxidative stress model. Experimental groups were treated with ZIF-8 or CCM@ZIF-8 NPs (co-incubated with H_2O_2-challenged BMSCs for 24 h).

For quantitative ROS profiling, cells were stained with 10 μmol/L fluorescent probe 2',7'-dichlorodihydrofluorescein diacetate (DCFH-DA; Beyotime) in serum-free medium (37 °C, 30 min, protected from light). The internalized probe was removed via three sequential washes with ice-cold PBS.

ROS distribution was captured using an all-in-one fluorescence microscope (BZ-X800, Keyence, Japan), and the fluorescence was quantified by ImageJ software. Single-cell resolution fluorescence quantification was subsequently performed on a CytoFLEX LX flow cytometer (Beckman Coulter, USA) with >10 000 events recorded per sample. Data were normalized to H_2O_2-treated controls and analyzed in FlowJo v10.8.1 (TreeStar, Ashland, OR, USA) using geometric mean fluorescence intensity (gMFI).

2.4.7 Alkaline phosphatase activity examination

To monitor the osteogenic effect on BMSCs, alkaline phosphatase (ALP) enzyme activity was measured. After seeding 1×10^5 cells per well in 12-well plates, they were cultured in osteogenic differentiation medium for 7 d, and then ALP staining was performed using the 5-bromo-4-chloro-3-indolyl phosphate/nitroblue tetrazolium (BCIP/NBT) Alkaline Phosphatase Color Development kit (Beyotime). The absorbance was measured at 520 nm to quantify ALP activity using the Alkaline Phosphatase Assay kit (Jiancheng Inc., China).

2.4.8 Tube formation assay

Tube formation assays were conducted using human umbilical vein endothelial cells (HUVECs), which were inoculated at a density of 5×10^4 cells per well on Matrigel for 12 h. Subsequently, after staining with ghost pen cyclic peptide (Biosharp, China), images were captured using a multifunctional fluorescence imaging system BZ-X800LE (Keens) to evaluate the tube-forming capacity, which was quantified using ImageJ software.

2.5 In vivo study

2.5.1 Ovariectomy model establishment

Thirty-two 8-week-old female C57BL/6J mice underwent bilateral ovariectomy (OVX) using established techniques as previously documented (Liu XF et al., 2024). Under aseptic conditions, their dorsal surfaces were sterilized with an iodine solution followed by medicinal alcohol, and the animals were secured in the prone position. Linear incisions of 10 mm were made bilaterally in the skin on the lumbar side, and both ovaries were carefully excised, with the oviducts ligated to prevent bleeding and ensure complete removal of ovarian tissue. The incisions were then closed with sutures, and post-operative care was provided according to institutional guidelines.

2.5.2 Bone defect creation and drug injection

Lithium phenyl-2,4,6-trimethylbenzoylphosphinate (LAP) powder was dissolved in PBS at 45 °C to obtain a 0.25% (2.5 g/L) photoinitiator solution. Subsequently, AlgMA (M301775) was added to the 0.25% (2.5 g/L) photoinitiator solution and heated at 65 °C for 30 min until the polymer completely dissolved. The solution was then infused with ZIF-8 NPs or CCM@ZIF-8 NPs. The mice were randomly divided into four groups eight weeks post-surgery: (1) blank, (2) AlgMA, (3) AlgMA@ZIF-8 hydrogel, and (4) AlgMA/CCM@ZIF-8 hydrogel. A bone defect with a diameter of 1 mm was created beneath the cartilage development plate in each mouse. The hydrogel formulations were respectively injected into the defect sites and immediately photocured in situ using a UV lamp at a wavelength of 405 nm for 30 s, ensuring rapid and efficient fixation for each group.

2.5.3 ROS level analysis of neutrophils in vivo

Quantitative assessment of neutrophil oxidative stress was performed via flow cytometric analysis in

femoral bone marrow from 16-week-old C57BL/6J mice, comparing controls (n=3) and osteoporotic models (n=3). Single-cell suspensions were prepared by mechanical dissociation and erythrocyte lysis (BD Pharm Lyse™, USA). Neutrophils were identified using the immunophenotypic markers cluster of differentiation 45 (CD45; BioLegend, USA; #147707), CD11b (BioLegend; #101225), and Ly6G (Cell Signaling, USA; #88876).

Intracellular superoxide levels were quantified by staining with dihydroethidium (DHE; Beyotime, S0064S) at 37 ℃ for 20 min (light-protected). Samples were analyzed on a CytoFLEX LX flow cytometer (Beckman Coulter). Data were analyzed in FlowJo v10.8.1 (TreeStar) using gMFI.

2.5.4 Micro-computerized tomography analysis

Animals were euthanized at two intervals (two or four weeks) after drug implantation, and femurs were extracted. The specimens were preserved in 4% (40 g/L) paraformaldehyde and then scanned using a micro-computerized tomography (micro-CT) system (Quantum GX, PerkinElmer, USA) to assess differences in the quality of bone healing. The scan parameters were: X-ray voltage, 80 kV; X-ray current, 100 μA; scan duration, 2 min; field of view, 36 mm; pixel dimension, 50 μm. The parameters of bone volume fraction (BV/TV), trabecular thickness (Tb.Th), and trabecular separation (Tb.Sp) were calculated.

2.5.5 Histological staining

Subsequently, histological evaluation was performed. Samples were decalcified using a 10% (100 g/L) ethylenediaminetetraacetic acid (EDTA) solution (Sigma-Aldrich, USA) with the solution changed twice weekly for at least eight weeks at 4 ℃ before embedding. Serial sections with a thickness of 5 μm were cut and mounted onto adhesion microscope slides (Citoglas, Beijing, China; Ref. 188105). Hematoxylin and eosin (H&E) and Masson's trichrome staining were conducted to observe bone regeneration.

For antigen retrieval, tissue sections were heated in sodium citrate buffer at 95 ℃ for 15 min. After cooling to room temperature, nonspecific binding sites were blocked with 5% (50 g/L) bovine serum albumin (BSA) in PBS for 1 h at room temperature. Primary antibody incubation was performed overnight at 4 ℃ using the following antibodies: 8-hydroxy-2'-deoxyguanosine (8-OHdG; MCE; HY-P81140), osterix (SP7; Abcam; ab22552), platelet endothelial cell adhesion molecule-1 (CD31; Abcam; ab182981), Runt-related transcription factor 2 (RUNX2; Abcam; ab192256), ALP (Invitrogen; PA5-106391), collagen type I α1 (COL1A1; Abcam; ab270993), and osteocalcin (OCN; Proteintech; 23418-1-AP). After washing with PBS, sections were incubated for 1 h at room temperature with Alexa Fluor® 555-conjugated goat anti-mouse IgG (Huabio; HA1118) for 8-OHdG and CD31 detection. iFluor™ 488-conjugated goat anti-rabbit IgG (Huabio; HA1121) for RUNX2, SP7, ALP, COL1A1, and OCN visualization. Following secondary antibody incubation, nuclei were counterstained with 4',6-diamidino-2-phenylindole dihydrochloride (DAPI; 1 μg/mL) for 5 min. Fluorescent images were acquired using an all-in-one fluorescence microscope (BZ-X800, Keyence).

2.6 Statistical analysis

All data are presented as mean±standard deviation (SD). Data in this study were obtained from at least three independent experiments (n≥3). To assess statistical differences, statistical analysis was performed using one-way analysis of variance (ANOVA), two-way ANOVA, or Student's t-test using SPSS 22.0 software (SPSS Inc., Chicago, IL, USA). Differences were considered statistically significant at P<0.05.

3 Results

3.1 Characterization of ROS-enriched microenvironment in osteoporotic bone marrow by scRNA-seq

Osteoporosis is a multifactorial age-related disease driven mainly by dysregulated interactions within the bone microenvironment (Yu and Wang, 2016). Through integrative analysis of scRNA-seq data from osteoporosis patients, we deciphered the complex cellular landscape of osteoporotic bone marrow. Notably, the osteoporotic bone microenvironment was found to harbor abundant immune cell subsets, while mesenchymal cell populations were significantly reduced (Figs. 2a and 2b), consistent with the clinical phenotypes of bone loss and chronic inflammation in osteoporosis patients. Among all the cell types, osteoblasts showed the most prominent ROS stress signature (Figs. 2c, 2d, and S1). Excessive ROS accumulation has been shown to compromise cell survival and impair osteogenic

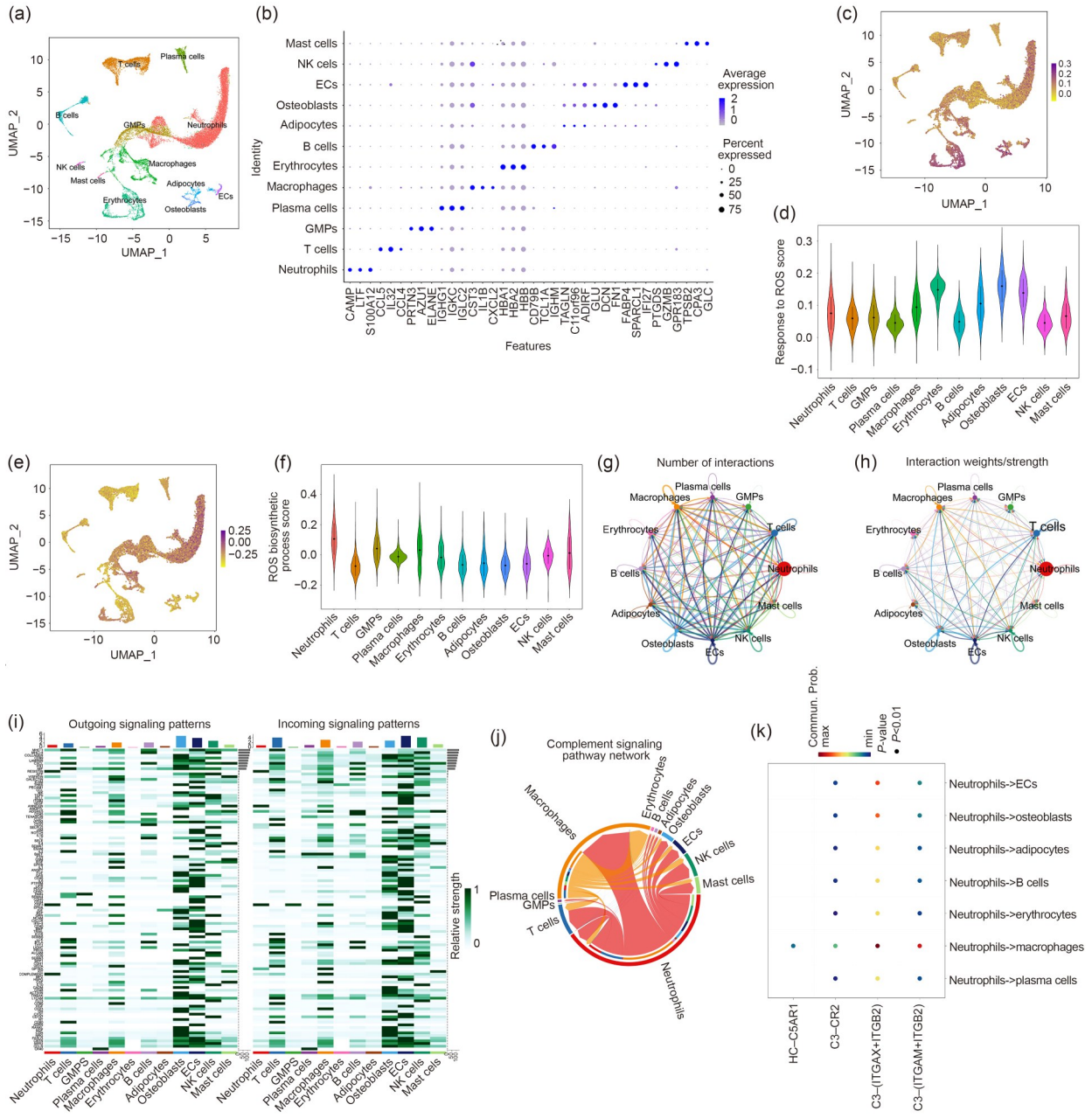

Fig. 2 Single-cell RNA-sequencing (scRNA-seq) analysis of reactive oxygen species (ROS)-enriched femoral microenvironment of osteoporosis patients. (a) Uniform Manifold Approximation and Projection (UMAP) illustrating the cellular composition of four osteoporotic femoral samples, colored by cell-type annotation. (b) Expression patterns of marker genes across distinct cell subpopulations. (c) UMAP visualization of "response to ROS" gene set enrichment scores. (d) Violin plots depicting the distribution of "response to ROS" gene set scores across cell clusters. (e) UMAP representation of "ROS biosynthetic process" gene set enrichment. (f) Violin plots showing "ROS biosynthetic process" gene set scores among different cell types. (g) Quantitative analysis of intercellular communication events between distinct cell populations. (h) Interaction weight matrix representing the strength of cellular crosstalk between different cell clusters. (i) Heatmap showing the intensity of incoming (right) and outgoing (left) signaling pathways across cell types. Rows represent signaling pathways, columns indicate cell populations, with darker hues denoting stronger pathway activation. (j) Chord diagram visualizing the complement signaling pathway networks between neutrophils and other cell populations. (k) Ligand–receptor pairs associated with complement signaling pathways originating from neutrophils to recipient cell clusters. GMPs: granulocyte-monocyte progenitors; ECs: endothelial cells; NK cells: natural killer cells; C5AR1: complement C5a receptor 1; C3: complement 3; CR2: complement receptor 2; ITGAX: integrin α X; ITGAM: integrin α M; ITGB2: integrin subunit β2; Commun. Prob.: communication probability.

differentiation (Manolagas, 2010; Zou et al., 2021; Tang et al., 2025). To identify cellular sources of ROS in the osteoporotic microenvironment, enrichment analysis of ROS synthesis-related gene sets was performed across all cell populations, revealing neutrophils as the primary contributors to ROS production (Figs. 2e and 2f). Consistent with the scRNA-seq findings, flow cytometry showed significantly increased ROS generation in osteoporotic neutrophils versus the control group (Fig. S2).

Cell–cell interaction analysis demonstrated intricate signaling networks between diverse immune cells and osteoblasts (Figs. 2g and 2h), highlighting the regulatory role of the immune microenvironment in osteoblast function. Further investigation of the specific signaling pathways mediating immune cell–osteoblast crosstalk (Fig. 2i) revealed that neutrophils potentially regulate osteoblast differentiation and fate determination through the complement-related signaling pathways (Figs. 2j and 2k). Importantly, these complement-associated pathways are closely linked to both the pro-inflammatory effects of neutrophils and their ROS production (Becker et al., 2024; Das et al., 2024; Maqsood et al., 2024). Furthermore, osteoblasts exhibit high expression of complement receptors, including complement C5a receptor 2 (C5AR2) and integrin subunit β2 (ITGB2) (Fig. S3), suggesting that neutrophil-derived C3a/C5a ligands regulate osteoblast function through specific ligand–receptor interactions. Critically, targeted blockade of C5a-mediated inflammation during early phases has been shown to enhance fracture healing (Kovtun et al., 2017). Collectively, these findings indicate that neutrophil-derived ROS in the osteoporotic microenvironment likely induce ROS stress in osteoblasts, exacerbating bone loss and accelerating disease progression. Therefore, therapeutic strategies targeting ROS accumulation in osteoblasts may represent a promising approach for mitigating osteoporosis.

3.2 Synthesis, characterization, and drug release kinetics of CCM@ZIF-8 NPs

CCM was encapsulated within ZIF-8 using a one-pot synthesis method, resulting in the formation of CCM@ZIF-8 NPs (Fig. 3a). During the fabrication process, the β-diketone groups of CCM coordinate with the Zn^{2+} of ZIF-8 and simultaneously form additional coordination bonds with 2-MIM (Jung et al., 2022). SEM and TEM images revealed that both ZIF-8 and CCM@ZIF-8 exhibit similar crystalline structures. However, CCM@ZIF-8 shows a rougher surface texture and slightly larger particle size due to the adsorption of CCM. The median particle diameters are about 25 nm for ZIF-8 NPs and 29 nm for CCM@ZIF-8 NPs (Fig. 3b).

FTIR analysis was conducted to investigate the chemical composition of CCM, ZIF-8, and CCM@ZIF-8 NPs (Fig. 3c). In the FTIR spectrum of CCM@ZIF-8 NPs, the characteristic peaks of CCM at 3512 cm^{-1} (attributed to the enol hydroxyl group) and 1512 cm^{-1} (corresponding to the phenolic hydroxyl group) were notably diminished (Perera et al., 2021). Additionally, a new peak emerged at about 420 cm^{-1}, indicative of the formation of a Zn−N bond (Nagaraju et al., 2017).

CCM@ZIF-8 and AlgMA/CCM@ZIF-8 exhibit pH-dependent release behavior, with enhanced dissolution at pH 5.5 (Figs. 3d and 3e), while hydrogel encapsulation significantly retards the release profile.

3.3 Biocompatibility of CCM@ZIF-8 NPs

CCK-8 cell viability/cytotoxicity tests on BMSCs were used to examine the biocompatibility of ZIF-8 and CCM@ZIF-8 NPs. Briefly, BMSCs were treated with specific concentration gradients of the prepared ZIF-8 and CCM@ZIF-8 NPs for 24 and 48 h. As shown in Fig. 4a, at concentrations below 20 μg/mL, there were no significant differences in BMSC viability between the control group and the group treated with ZIF-8 or CCM@ZIF-8 NPs, for both the 24 and 48 h incubation periods. Therefore, 20 μg/mL was selected as the optimal concentration for the subsequent in vitro and in vivo studies.

When BMSCs and RAW264.7 cells were treated with CCM@ZIF-8 NPs at 20 μg/mL for 24 h, the live/dead staining results provided visual evidence of their biocompatibility. Most cells exhibited green fluorescence, indicating high viability, while only negligible red fluorescence was observed, suggesting low levels of cell death (Fig. 4b). These findings confirm that CCM@ZIF-8 NPs are biocompatible and safe for further in vitro and in vivo studies. Next, to verify whether CCM@ZIF-8 NPs could be effectively internalized by cells, we used BMSCs and RAW264.7 to investigate the intracellular uptake of CCM@ZIF-8 NPs using confocal microscopy. After a 24 h incubation period, green fluorescence was clearly observed within both BMSCs (Fig. 5a) and RAW264.7 (Fig. 5b), which indicates

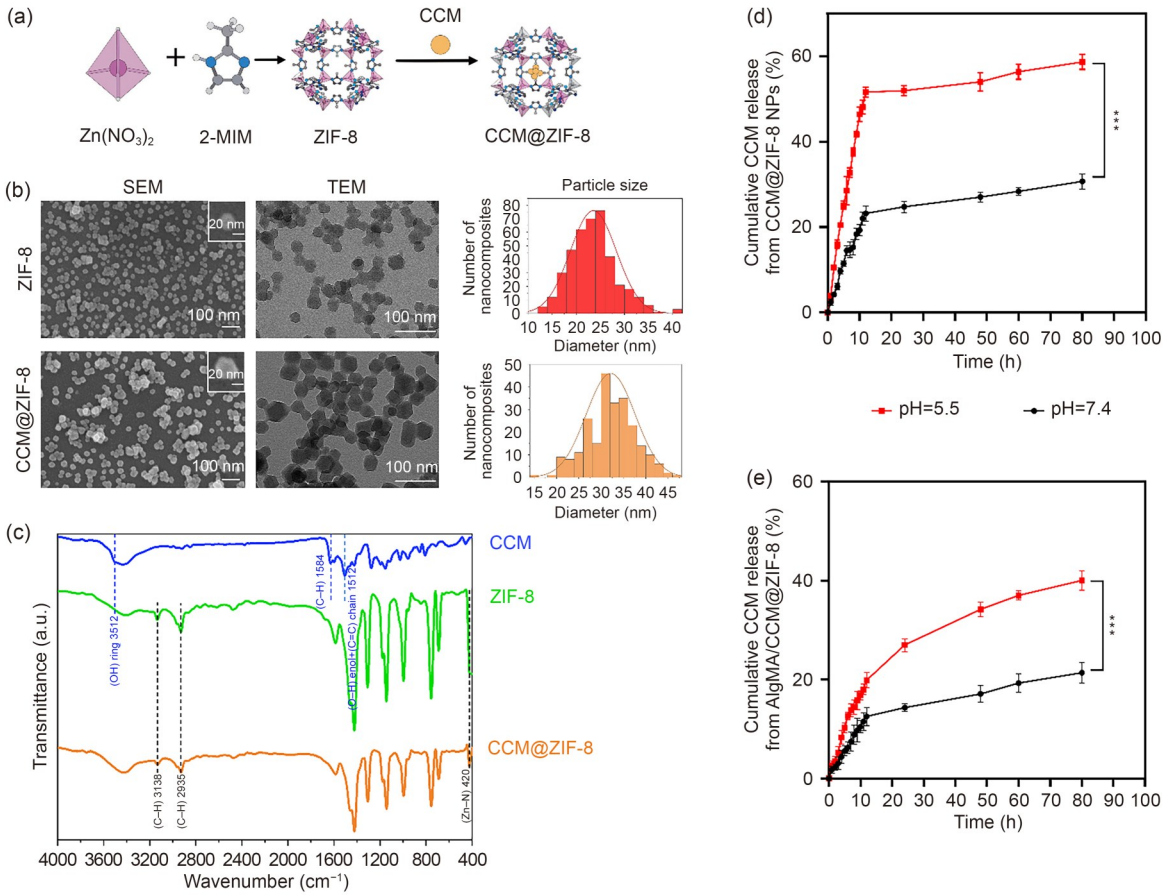

Fig. 3 Characterization of zeolitic imidazolate framework-8 (ZIF-8) and curcumin-encapsulated ZIF-8 (CCM@ZIF-8) nanoparticles (NPs). (a) Schematic illustration of the synthesis process for ZIF-8 and CCM@ZIF-8 NPs. (b) Scanning electron microscopy (SEM) and transmission electron microscopy (TEM) images, along with particle size distribution of ZIF-8 and CCM@ZIF-8 NPs. The inset provides a local magnification. (c) Fourier-transform infrared (FTIR) spectra in the range of 4000–400 cm^{-1} for CCM, ZIF-8, and CCM@ZIF-8. (d) Cumulative CCM release from CCM@ZIF-8 under different pH conditions. (e) Cumulative CCM release from AlgMA/CCM@ZIF-8 under different pH conditions. (d, e) Data are expressed as mean±standard deviation (SD) (n=3). *** P<0.001. 2-MIM: 2-methylimidazole; AlgMA: alginate methacrylate; a.u.: arbitrary unit.

successful cellular uptake of the CCM@ZIF-8 NPs (Li Y et al., 2024). The results show that CCM@ZIF-8 NPs can efficiently penetrate and be internalized by the cells, suggesting their potential for enhanced intracellular delivery and therapeutic efficacy.

3.4 Reduction of intracellular ROS levels by CCM@ZIF-8 NPs in BMSCs

To assess the antioxidant efficacy of CCM@ZIF-8 NPs on BMSCs, intracellular ROS levels were quantitatively measured using the fluorescent probe DCFH-DA. Figs. 6a and 6b show that treatment with 500 μmol/L H_2O_2 induced a significant elevation in fluorescence intensity (P<0.001) compared to untreated controls, whereas CCM@ZIF-8 NP cotreatment markedly attenuated this increase (P<0.001). Flow cytometry further confirmed these findings, demonstrating that CCM@ZIF-8 NPs reduced intracellular ROS levels by approximately 50% relative to both H_2O_2-treated and H_2O_2+ZIF-8-treated control groups (P<0.001; Figs. 6c and 6d). The alleviation of ROS by CCM@ZIF-8 NPs may be mediated by the upregulation of the antioxidant transcription factor NRF2 (Fig. S4). These results collectively indicate that CCM@ZIF-8 NPs effectively mitigate oxidative stress in BMSCs.

3.5 Inhibition of osteoclast formation and marker expression by CCM@ZIF-8 NPs

RAW264.7 cells were cultured in osteoclastic differentiation medium to assess the impact of CCM@ZIF-8 NPs on osteoclast development. Results showed that CCM@ZIF-8 NPs significantly inhibited

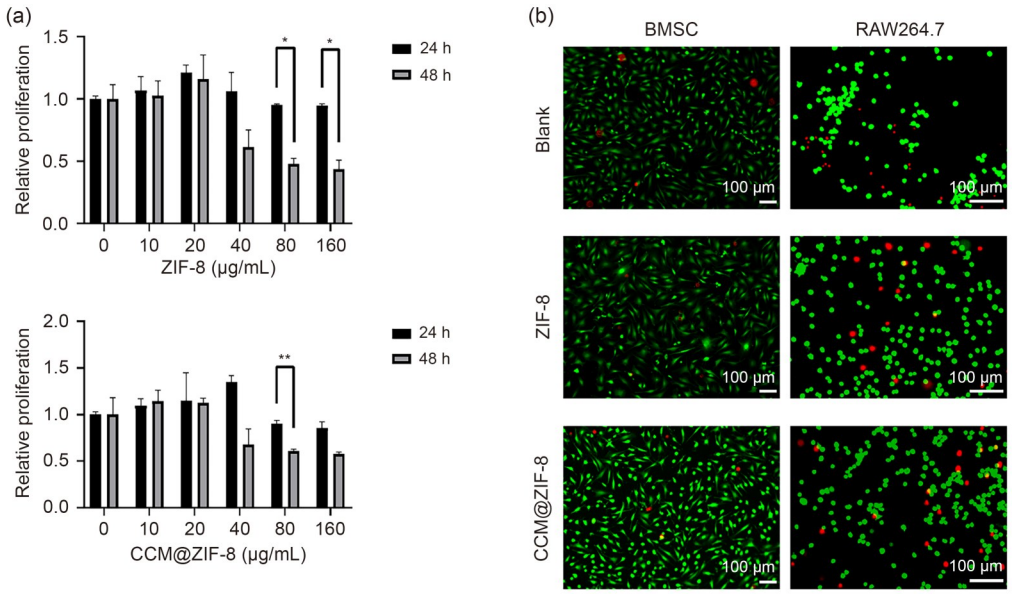

Fig. 4 Drug concentration screening and biocompatibility evaluation of zeolitic imidazolate framework-8 (ZIF-8) and curcumin-encapsulated ZIF-8 (CCM@ZIF-8) nanoparticles (NPs). (a) Proliferation of bone marrow-derived mesenchymal stem cells (BMSCs) cocultured with ZIF-8 or CCM@ZIF-8 NPs. (b) Fluorescence microscopy images of live/dead staining for BMSCs and mouse mononuclear macrophage cells (RAW264.7) after coculturing with ZIF-8 or CCM@ZIF-8 NPs for 24 h. Calcein acetoxymethyl ester (green fluorescence) for live cells and ethidium homodimer-1 (red fluorescence) for dead cells. Data are expressed as mean±standard deviation (SD) (n=3). * P<0.05, ** P<0.01.

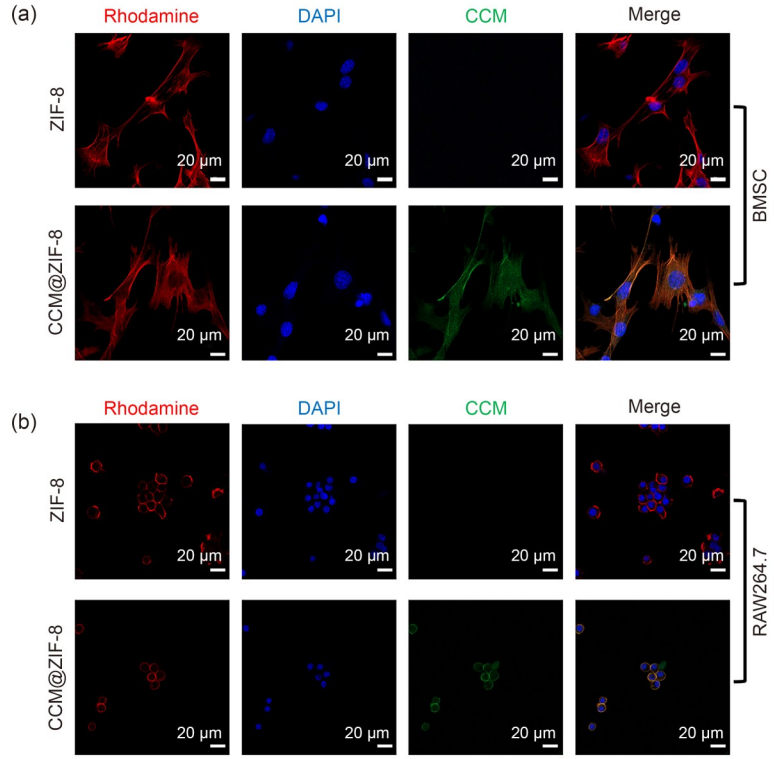

Fig. 5 Cellular internalization of curcumin-encapsulated zeolitic imidazolate framework-8 nanoparticles (CCM@ZIF-8 NPs). (a, b) Confocal microscopy images of bone marrow-derived mesenchymal stem cells (BMSCs) (a) and mouse mononuclear macrophage cells (RAW264.7) (b) after coculturing with ZIF-8 or CCM@ZIF-8 NPs for 24 h. DAPI: 4',6-diamidino-2'-phenylindole.

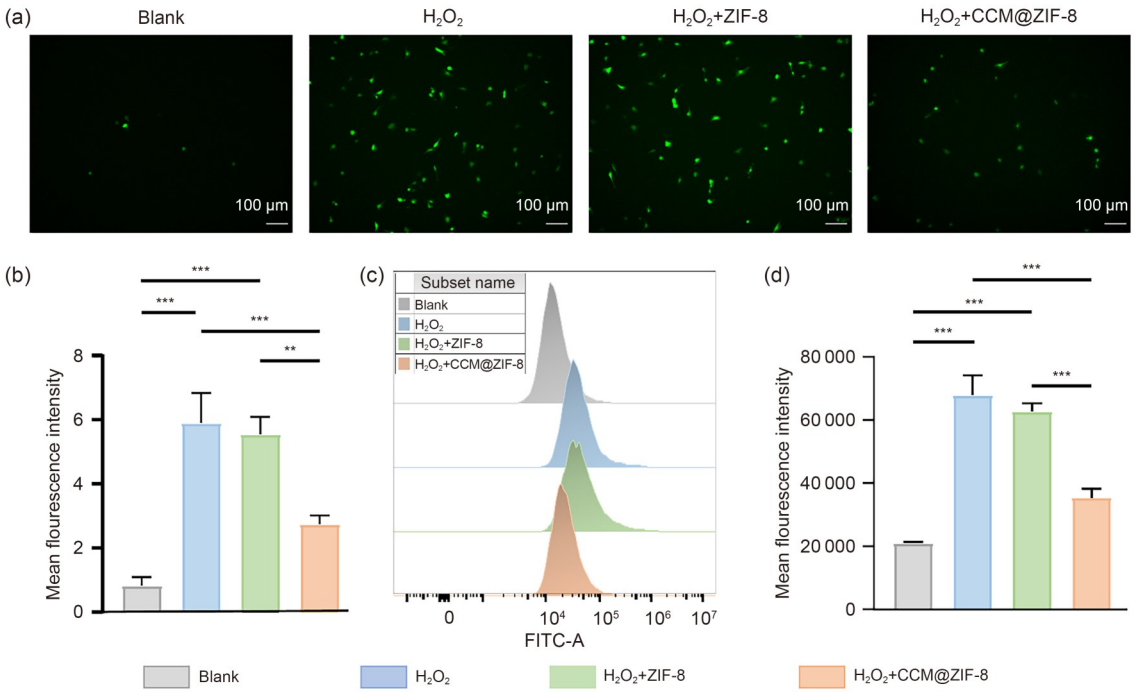

Fig. 6 Effect of curcumin-encapsulated zeolitic imidazolate framework-8 nanoparticles (CCM@ZIF-8 NPs) on H_2O_2-induced reactive oxygen species (ROS) generation in bone marrow-derived mesenchymal stem cells (BMSCs). (a) Representative fluorescence micrographs of intracellular ROS detection using dichlorodihydrofluorescein diacetate (DCFH-DA) staining in BMSCs under different treatment conditions. (b) Quantitative analysis of relative fluorescence intensity from panel (a). (c) Flow cytometric histograms showing intracellular ROS levels. (d) Quantitative analysis of mean fluorescence intensity from flow cytometry data. Data are expressed as mean±standard deviation (SD) (n=3). ** P<0.01, *** P<0.001. FITC: fluorescein isothiocyanate.

osteoclast formation compared to both the ZIF-8 NP-treated and control groups (P<0.001), as shown by TRAP staining (Fig. 7a).

To further elucidate the role of CCM@ZIF-8 NPs in osteoclastogenesis, we quantified the expression levels of messenger RNA (mRNA) involved in osteoclast differentiation using RT-PCR. Fig. 7b shows that treatment with CCM@ZIF-8 NPs significantly reduced the mRNA expression levels of genes associated with osteoclast differentiation, including *TRAP* (P<0.001), *Ctsk* (P<0.05), and *c-Fos* (P<0.01). These findings indicate that CCM@ZIF-8 NPs exert a negative regulatory effect on osteoclast differentiation and downregulate the expression of osteoclastogenesis-related genes.

3.6 Promotion of osteogenesis and angiogenesis by CCM@ZIF-8 NPs in vitro

ALP staining showed that the CCM@ZIF-8 NP treatment group exhibited significantly stronger ALP activity in BMSCs compared to the control group (P<0.05; Fig. 8a), indicating that CCM@ZIF-8 NPs effectively stimulate the production of ALP, a marker of osteogenic differentiation, highlighting their capability in promoting osteogenesis (Sun et al., 2022).

The pro-angiogenic potential of CCM@ZIF-8 NPs was confirmed using a tube formation assay with HUVECs. After 12 h culture, the total tube length in the CCM@ZIF-8 NP-treated group was significantly increased compared to the control and ZIF-8 NP groups (P<0.05; Fig. 8b), suggesting that CCM@ZIF-8 NPs can effectively promote angiogenesis in vitro, which is essential for large-area bone reconstruction (Lee et al., 2023).

3.7 Promotion of bone healing by CCM@ZIF-8 NPs in OVX-induced osteoporotic mouse model

To further assess the therapeutic effects of CCM@ZIF-8 NPs in vivo, we used a typical OVX-induced osteoporotic mouse model (Fig. 9a). No adverse events or fatalities were recorded in any of the experimental groups. Eight weeks post-OVX surgery, bone defects with a diameter of 1 mm were created in each femur. Immediately after defect creation, the corresponding drugs were injected into the bone defect area

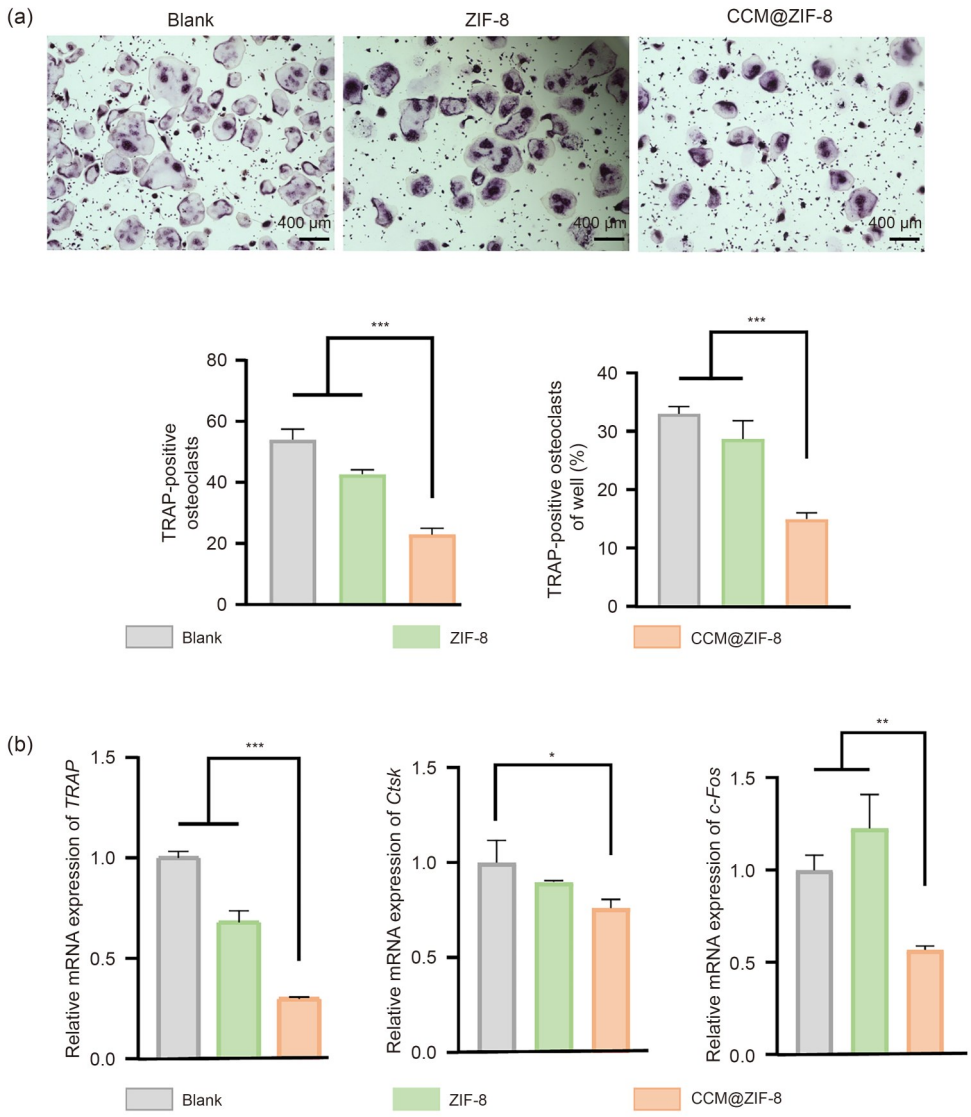

Fig. 7 Inhibition of osteoclast formation and gene expression by curcumin-encapsulated zeolitic imidazolate framework-8 nanoparticles (CCM@ZIF-8 NPs) in vitro. (a) Representative images and quantification of tartrate-resistant acid phosphatase (TRAP)-positive multinucleated cells. (b) The expression levels of *TRAP*, *Ctsk*, and *c-Fos* messenger RNAs (mRNAs) were quantitatively analyzed by real-time polymerase chain reaction (RT-PCR). Data are expressed as mean± standard deviation (SD) (*n*=3). * *P*<0.05, ** *P*<0.01, *** *P*<0.001. *Ctsk*: cathepsin K; *c-Fos*: cellular proto-oncogene *fos*.

for each group. Mice were sacrificed in batches after two or four weeks following drug injection surgery. Femurs were harvested for micro-CT scanning and staining. The CT scans revealed that CCM@ZIF-8 NPs promoted bone healing at the defect area compared to the other three groups (Fig. 9b). Fig. 9c shows that quantitative analysis confirmed a significant increase in BV/TV in the CCM@ZIF-8 NP-treated group relative to the groups without CCM@ZIF-8 NP treatment at both two weeks (P<0.01) and four weeks (P< 0.001). Additionally, a significant increase in Tb.Th was observed in the CCM@ZIF-8 NP-treated group compared to the blank group at four weeks (P<0.05). H&E and Masson's trichrome staining of femur tissue sections also verified that CCM@ZIF-8 NPs accelerated bone healing in OVX model mice (Figs. 10a and 10b). Immunofluorescence staining for 8-OHdG confirmed superior ROS-scavenging capacity in the CCM@ZIF-8 NP-treated group (Fig. 10c), while concurrent detection of RUNX2 (Fig. 10d) and CD31 (Fig. 10e) demonstrated enhanced bone regeneration and vascularization (Wang Z et al., 2024) within the

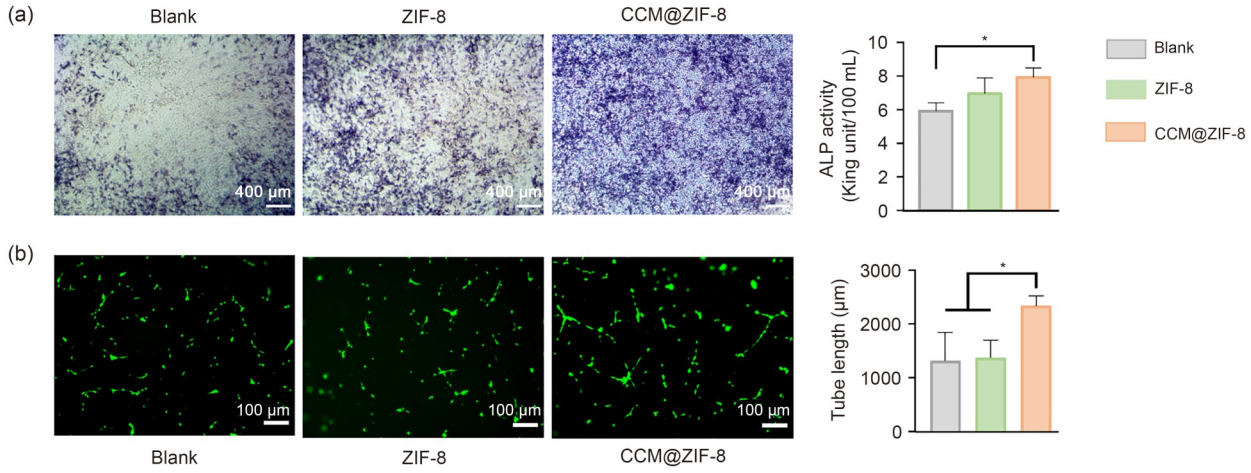

Fig. 8 Promotion of osteogenesis and vascularization by curcumin-encapsulated zeolitic imidazolate framework-8 nanoparticles (CCM@ZIF-8 NPs) in vitro. (a) Representative images and statistical analysis of alkaline phosphatase (ALP) staining after coculturing for 7 d. 1 King unit=0.17 IU. (b) Representative fluorescence microscopy images and statistical analysis of tube formation after coculturing for 12 h. Data are expressed as mean±standard deviation (SD) (n=3). * P<0.05.

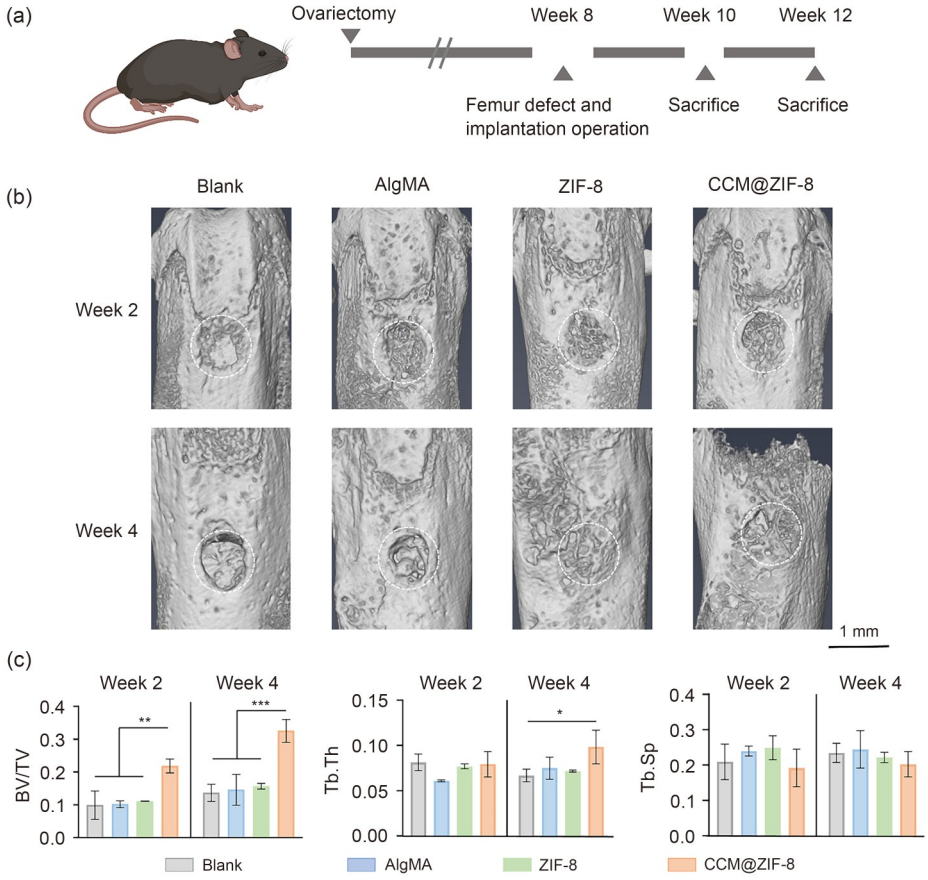

Fig. 9 Promotion of bone healing by curcumin-encapsulated zeolitic imidazolate framework-8 nanoparticles (CCM@ZIF-8 NPs) in osteoporotic mouse model. (a) Schematic of ovariectomy, bone defect and implantation operation, and subsequent steps for in vivo evaluation. (b) Three-dimensional (3D) micro-computerized tomography (micro-CT) reconstructions of defect sites two and four weeks post-implantation. (c) Quantification of bone morphological parameters bone volume fraction (BV/TV), trabecular thickness (Tb.Th), and trabecular separation (Tb.Sp). Data are expressed as mean±standard deviation (SD) (n=4). * P<0.05, ** P<0.01, *** P<0.001. AlgMA: alginate methacrylate.

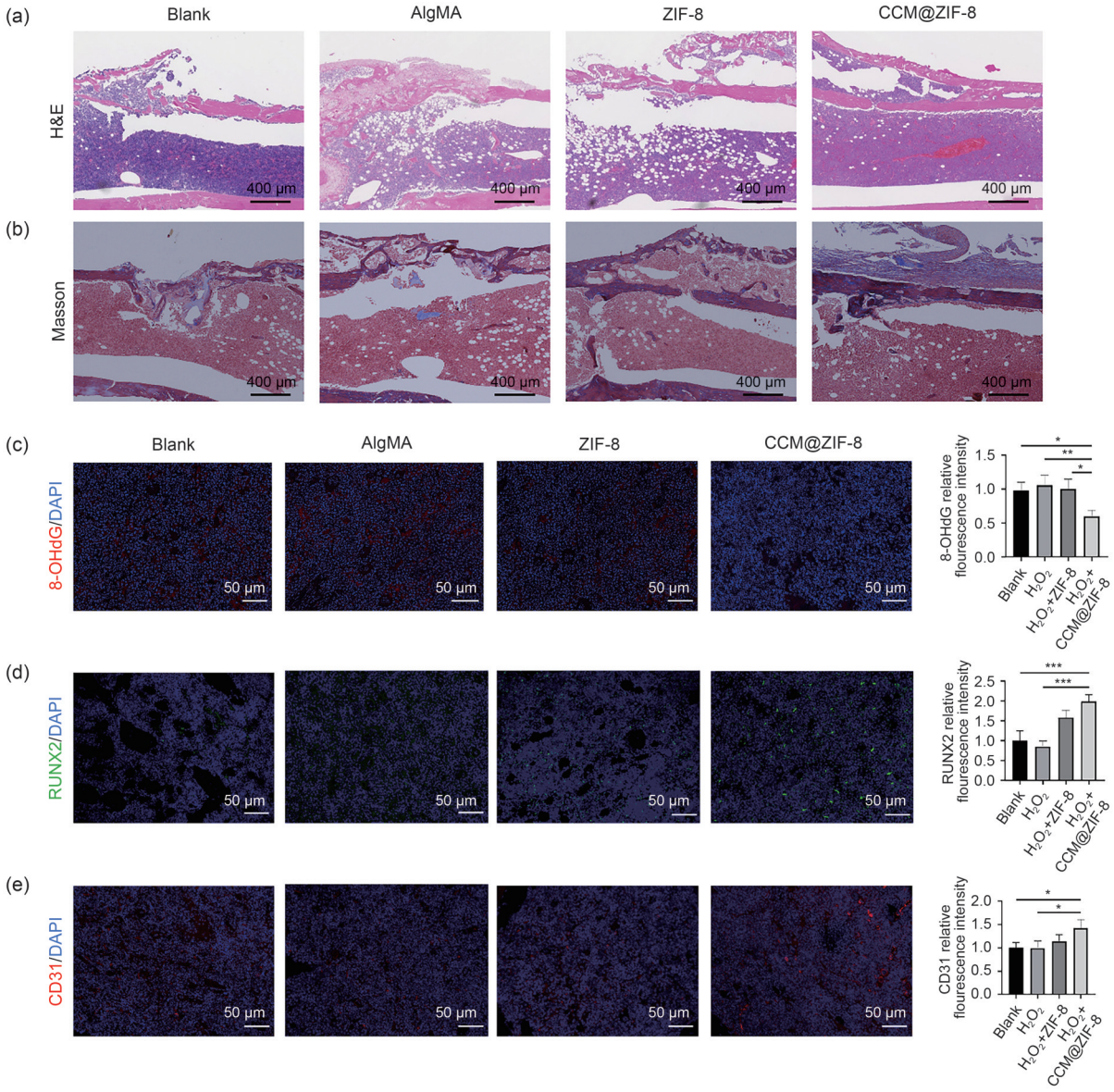

Fig. 10 Facilitation of bone and vascular regeneration by curcumin-encapsulated zeolitic imidazolate framework-8 nanoparticles (CCM@ZIF-8 NPs) in osteoporotic mouse model. (a, b) Hematoxylin and eosin (H&E) staining (a) and Masson's trichrome staining (b) of the surgical area in osteoporotic mice four weeks after drug implantation. (c–e) Representative immunofluorescence staining of 8-hydroxy-2'-deoxyguanosine (8-OHdG) (c), Runt-related transcription factor 2 (RUNX2) (d), and platelet endothelial cell adhesion molecule-1 (CD31) (e) of the surgical area in osteoporotic mice four weeks after drug implantation and their quantitative analysis of mean fluorescence intensity. Data are expressed as mean±standard deviation (SD) (n=3). * P<0.05, ** P<0.01, *** P<0.001. AlgMA: alginate methacrylate; DAPI: 4',6-diamidino-2-phenylindole.

defect area following CCM@ZIF-8 NP treatment. Detection of COL1A1, ALP, OCN, and SP7 also confirmed the enhanced bone regeneration in the CCM@ZIF-8 NP-treated group (Fig. S5). These findings show that CCM@ZIF-8 NPs can effectively promote bone healing and improve bone quality in the OVX-induced osteoporosis mouse model.

4 Discussion

The treatment of bone defects in osteoporotic patients remains a major clinical challenge (The Lancet Diabetes & Endocrinology, 2021). Our scRNA-seq analysis of human osteoporotic tissues provides critical insights into the mechanistic interplay between ROS

dynamics and osteoblast dysfunction. While osteoblasts showed profound ROS stress signatures, their limited expression of ROS synthesis-related genes strongly suggests an exogenous origin of ROS overload, likely originating from neighboring immune cells within the bone marrow niche. This observation aligns with emerging evidence implicating immune-metabolic crosstalk in bone remodeling disorders (Su et al., 2022). Notably, our scRNA-seq analysis identified neutrophils as the predominant source of ROS within the osteoporotic bone marrow niche, with persistent activation of complement-mediated intercellular signaling pathways between neutrophils and osteoblasts. This finding carries significant dual-pathway implications. First, complement system activation in neutrophils drives ROS overproduction (Morris et al., 2022; Das et al., 2024; Maqsood et al., 2024), establishing a prooxidant microenvironment that directly suppresses osteogenic capacity (Sheng et al., 2023; Yang Z et al., 2023; Liu J et al., 2024; Chen W et al., 2025). Second, neutrophil-derived inflammatory signals, potentially mediated by complement pathways, may synergistically exacerbate osteoblast apoptosis and differentiation arrest (Zou et al., 2021). This two-pronged mechanism, combining oxidative stress and chronic inflammation, could explain the accelerated bone loss observed in advanced osteoporosis. These findings collectively underscore the therapeutic potential of targeting ROS accumulation in BMSCs for osteoporotic bone healing.

Consequently, developing effective strategies to modulate the ROS-enriched, osteogenesis-inhibitory bone marrow microenvironment in osteoporosis patients remains a critical unmet challenge for achieving functional bone defect regeneration (Guo et al., 2023). CCM, a natural polyphenol derived from the rhizomes of *Curcuma longa* (a traditional Chinese medicinal herb), has emerged as a promising therapeutic agent for bone regeneration due to its potent ROS-scavenging properties and osteogenic effects (Tan et al., 2021; Wang et al., 2025). However, the clinical translation of CCM for osteoporosis-related bone repair is significantly hindered by its poor pharmacokinetic profile, including extremely low aqueous solubility, limited systemic bioavailability, and rapid hepatic metabolism and elimination (Inchingolo et al., 2024). These pharmacological challenges underscore the critical need for developing advanced delivery systems that can both protect CCM from premature degradation and ensure its sustained release at bone defect sites.

In this study, we developed an innovative microenvironment-responsive therapeutic platform by integrating CCM@ZIF-8 NPs within AlgMA hydrogel for targeted osteoporosis treatment. This system aims to ameliorate the local ROS-enriched, osteo-inhibitory microenvironment, reduce ROS stress in osteoblasts, and enhance their survival and osteogenic capacity. The AlgMA hydrogel component serves as an injectable, photopolymerizable scaffold that perfectly adapts to complex bone defect geometries while providing a bioactive matrix for cellular attachment and tissue regeneration (Aycan et al., 2024). The embedded ZIF-8 NPs exhibit intelligent pH-responsive behavior, undergoing controlled degradation in the acidic microenvironment characteristic of osteoporotic bone (Chen LF et al., 2025), which is mediated by osteoclast-derived hydrogen ions. This microenvironment-triggered dissolution enables spatiotemporal release of CCM, achieving therapeutic local concentrations while minimizing systemic exposure. This strategy avoids the systemic effects associated with conventional oral osteoporosis medications such as alendronate. By synergistically combining AlgMA's structural support with ZIF-8's stimuli-responsive drug release properties, our system demonstrates a novel strategy for precision treatment of osteoporotic bone defects through: (1) on-demand antioxidant delivery, (2) osteoblast protection, and (3) creation of a regenerative niche. This platform represents a significant advance in developing pathophysiology-driven biomaterials for complex bone regeneration challenges.

Our study revealed that elevated ROS levels constitute a defining feature of the osteoporotic bone marrow microenvironment, where CCM@ZIF-8 NPs show potent ROS-scavenging and bone-regenerative capabilities. ROS-associated oxidative stress exerts cytotoxic effects on osteoblasts, inducing apoptosis (Li et al., 2021). Concurrently, ROS impairs BMSC osteogenic differentiation by suppressing β-catenin signaling through Forkhead box O (FOXO)-mediated inhibition of the Wingless/integrated (WNT) pathway (Almeida et al., 2009). As the master regulator of antioxidant responses, NRF2 maintains ROS homeostasis and prevents oxidative damage (Wang et al., 2023). Under physiological conditions, cytoplasmic Kelch-like ECH-associated protein 1 (KEAP1) sequesters NRF2, maintaining low basal levels. During oxidative stress, activated NRF2 translocates to the nucleus where it transcriptionally controls virtually all antioxidant response elements

(AREs) (Dodson et al., 2019), inducing downstream antioxidant enzymes and conferring cytoprotection (Morgenstern et al., 2024). CCM disrupts NRF2–KEAP1 binding through conformational alteration of KEAP1 (Shin et al., 2020), thereby enhancing NRF2 nuclear translocation and ROS clearance. This mechanism alleviates ROS-mediated suppression of osteogenic differentiation. Thus, CCM@ZIF-8 NPs may promote osteogenesis by both restoring BMSC viability through ROS mitigation and reversing the osteo-inhibitory microenvironment imposed by oxidative stress.

Overreaction of osteoclasts is one of the contributors to osteoporotic bone resorption. Mature osteoclasts attach to the bone surface and secrete a large number of H^+ ions, thereby acidifying the local extracellular microenvironment (Boyle et al., 2003; Tsukasaki and Takayanagi, 2019). This acidic environment dissolves the bone's mineral phase and creates ideal conditions for the breakdown of the organic matrix by *TRAP* and *Ctsk* (Lin et al., 2020). Our results showed that CCM@ZIF-8 NPs reduced osteoclast formation and activity by downregulating osteoclastogenesis-related markers (*TRAP*, *Ctsk*, and *c-Fos*) during osteoclast differentiation.

Thus, the bifunctional activity of AlgMA/CCM@ZIF-8 nanocomposite hydrogel targets both osteoblasts and osteoclasts, not only attenuating excessive bone resorption but also actively enhancing bone formation. This dual-action approach represents a significant advance in osteoporosis therapy. Future investigations should delineate the tripartite interplay among neutrophils, the complement system, and ROS generation, as well as their collective impact on osteoporotic pathogenesis, to provide a more comprehensive mechanistic understanding.

5 Conclusions

This study reveals a key mechanism in osteoporosis pathogenesis whereby neutrophil-derived ROS generate severe oxidative stress in osteoblasts, compromising their function through complement activation pathways. This ROS-mediated disruption of bone microenvironment homeostasis critically impairs the regenerative capacity of osteoporotic bone defects. The engineered AlgMA/CCM@ZIF-8 nanocomposite hydrogel targets ROS accumulation in BMSCs and effectively promotes osteoporotic bone repair through the multifaceted mechanism: (1) regulating BMSC fate determination via ROS scavenging, and (2) synergistically suppressing osteoclastogenesis. These findings not only elucidate the crucial role of ROS signaling in osteoporosis pathogenesis but also establish the AlgMA/CCM@ZIF-8 nanocomposite hydrogel as a promising therapeutic platform for regenerating osteoporotic bone defects, providing a foundational strategy for developing ROS-targeted nanocomposites in bone tissue engineering.

Data availability statement

The single-cell RNA sequencing data analyzed in this study were obtained from the Gene Expression Omnibus (GEO; https://www.ncbi.nlm.nih.gov/geo) under accession number GSE169396. The original contributions presented in the study are included in the article; further inquiries can be directed to the corresponding authors.

Acknowledgments

This work was supported by the Zhejiang Traditional Chinese Medicine Administration Program (No. 2023ZL242) and the Zhejiang Provincial Medical and Health Science and Technology Program (No. 2023KY035), China.

Author contributions

Wei HU and Feiya ZHAO contributed to the conceptualization, methodology, software, visualization, writing – original draft, and writing – review & editing. Wei HU, Tianyi FEI, and Zhichao LIU contributed to the data curation, formal analysis, investigation, and validation. Mengfei YU, Yude DING, Fan YANG, and Feiya ZHAO contributed to the resources, supervision, writing – review & editing, project administration, and funding acquisition. All authors have read and approved the final manuscript, and therefore, they have full access to all the data in the study and take responsibility for the integrity and security of the data.

Compliance with ethics guidelines

Wei HU, Tianyi FEI, Zhichao LIU, Yude DING, Mengfei YU, Fan YANG, and Feiya ZHAO declare that they have no conflicts of interest.

All institutional and national guidelines for the care and use of laboratory animals were followed. The study was approved by the Ethics Committee of Zhejiang Provincial People's Hospital (No. 20230526174010377463).

References

Almeida M, Ambrogini E, Han L, et al., 2009. Increased lipid oxidation causes oxidative stress, increased peroxisome proliferator-activated receptor-γ expression, and diminished

pro-osteogenic Wnt signaling in the skeleton. *J Biol Chem*, 284(40):27438-27448. https://doi.org/10.1074/jbc.M109.023572

Amaroli A, Panfoli I, Bozzo M, et al., 2024. The bright side of curcumin: a narrative review of its therapeutic potential in cancer management. *Cancers (Basel)*, 16(14):2580. https://doi.org/10.3390/cancers16142580

Au-Duong AN, Lee CK, 2017. Iodine-loaded metal organic framework as growth-triggered antimicrobial agent. *Mater Sci Eng C*, 76:477-482. https://doi.org/10.1016/j.msec.2017.03.114

Aycan D, Gül İ, Yorulmaz V, et al., 2024. Gelatin microsphere-alginate hydrogel combined system for sustained and gastric targeted delivery of 5-fluorouracil. *Int J Biol Macromol*, 255:128022. https://doi.org/10.1016/j.ijbiomac.2023.128022

Barbour KE, Lui LY, Ensrud KE, et al., 2014. Inflammatory markers and risk of hip fracture in older white women: the study of osteoporotic fractures. *J Bone Miner Res*, 29(9): 2057-2064. https://doi.org/10.1002/jbmr.2245

Becker S, Swoboda A, Siemer H, et al., 2024. Membrane potential dynamics of C5a-stimulated neutrophil granulocytes. *Pflugers Arch*, 476(6):1007-1018. https://doi.org/10.1007/s00424-024-02947-8

Boyle WJ, Simonet WS, Lacey DL, 2003. Osteoclast differentiation and activation. *Nature*, 423:337-342. https://doi.org/10.1038/nature01658

Chen JY, Hao ZW, Li HK, et al., 2024. Osteoporotic osseointegration: therapeutic hallmarks and engineering strategies. *Theranostics*, 14(10):3859-3899. https://doi.org/10.7150/thno.96516

Chen LF, Wang Y, Huang XQ, et al., 2025. Maltodextrin-driven MOF nano-antibacterial system for effective targeted bacteria and enhancing photodynamic therapy in bacterial keratitis. *J Control Release*, 380:1164-1183. https://doi.org/10.1016/j.jconrel.2025.02.031

Chen W, Pan YF, Chu CH, et al., 2025. Microenvironment-responsive nanoparticles functionalized titanium implants mediate redox balance and immunomodulation for enhanced osseointegration. *Mater Today Bio*, 31:101628. https://doi.org/10.1016/j.mtbio.2025.101628

Cho J, Feldman G, Tomlinson R, et al., 2024. Medication-related osteonecrosis of the jaw (MRONJ) systemic review: mevalonate pathway mechanisms explored. *Oral Surg Oral Med Oral Pathol Oral Radiol*, 138(4):475-483. https://doi.org/10.1016/j.oooo.2024.05.014

Das D, Thacker H, Priya K, et al., 2024. Complement component 5a receptor 1 and leukotriene B4 receptor 1 regulate neutrophil extracellular trap (NET) formation through Rap1a/B-Raf/ERK signaling pathway and their deficiency in term low birth weight newborns leads to deficient NETosis. *Int Immunopharmacol*, 142:113165. https://doi.org/10.1016/j.intimp.2024.113165

de Oliveira PGFP, Bonfante EA, Bergamo ETP, et al., 2020. Obesity/metabolic syndrome and diabetes mellitus on peri-implantitis. *Trends Endocrinol Metab*, 31(8):596-610. https://doi.org/10.1016/j.tem.2020.05.005

Dodson M, Castro-Portuguez R, Zhang DD, 2019. NRF2 plays a critical role in mitigating lipid peroxidation and ferroptosis. *Redox Biol*, 23:101107. https://doi.org/10.1016/j.redox.2019.101107

Guan HT, Wang W, Jiang ZC, et al., 2024. Magnetic aggregation-induced bone-targeting nanocarrier with effects of piezo1 activation and osteogenic-angiogenic coupling for osteoporotic bone repair. *Adv Mater*, 36(13):e2312081. https://doi.org/10.1002/adma.202312081

Guo QH, Yang SS, Ni GQ, et al., 2023. The preparation and effects of organic-inorganic antioxidative biomaterials for bone repair. *Biomedicines*, 12:70. https://doi.org/10.3390/biomedicines12010070

Huang ZY, Jiang XZ, Zhang LC, et al., 2025. Multifunctional manganese-based nanogels catalyze immune energy metabolism to promote bone repair. *Compos B Eng*, 291:112005. https://doi.org/10.1016/j.compositesb.2024.112005

Iantomasi T, Romagnoli C, Palmini G, et al., 2023. Oxidative stress and inflammation in osteoporosis: molecular mechanisms involved and the relationship with microRNAs. *Int J Mol Sci*, 24(4):3772. https://doi.org/10.3390/ijms24043772

Inchingolo F, Inchingolo AD, Latini G, et al., 2024. The role of curcumin in oral health and diseases: a systematic review. *Antioxidants (Basel)*, 13(6):660. https://doi.org/10.3390/antiox13060660

Jung S, Chang S, Kim NE, et al., 2022. Curcumin/zeolitic imidazolate framework-8 nanoparticle-integrated microneedles for pH-responsive treatment of skin disorders. *ACS Appl Nano Mater*, 5(9):13671-13679. https://doi.org/10.1021/acsanm.2c03884

Kovtun A, Bergdolt S, Hägele Y, et al., 2017. Complement receptors C5aR1 and C5aR2 act differentially during the early immune response after bone fracture but are similarly involved in bone repair. *Sci Rep*, 7:14061. https://doi.org/10.1038/s41598-017-14444-3

The Lancet Diabetes & Endocrinology, 2021. Osteoporosis: overlooked in men for too long. *Lancet Diabetes Endocrinol*, 9(1):1. https://doi.org/10.1016/s2213-8587(20)30408-3

Lee SH, Lee KG, Lee J, et al., 2023. Three-dimensional kagome structures in a PCL/HA-based hydrogel scaffold to lead slow BMP-2 release for effective bone regeneration. *Bio-Des Manuf*, 6:12-25. https://doi.org/10.1007/s42242-022-00219-x

Li SW, Lin YH, Mo CZ, et al., 2024. Application of metal-organic framework materials in regenerative medicine. *J Mater Chem B*, 12(35):8543-8576. https://doi.org/10.1039/d4tb00226a

Li X, Li BE, Shi Y, et al., 2021. Targeting reactive oxygen species in stem cells for bone therapy. *Drug Discov Today*, 26(5):1226-1244. https://doi.org/10.1016/j.drudis.2021.03.002

Li X, Sung P, Zhang D, et al., 2023. Curcumin in vitro neuroprotective effects are mediated by p62/keap-1/Nrf2 and PI3K/AKT signaling pathway and autophagy inhibition.

Physiol Res, 72(4):497-510.
https://doi.org/10.33549/physiolres.935054

Li Y, Cai ZW, Ma WJ, et al., 2024. A DNA tetrahedron-based ferroptosis-suppressing nanoparticle: superior delivery of curcumin and alleviation of diabetic osteoporosis. *Bone Res*, 12:14.
https://doi.org/10.1038/s41413-024-00319-7

Lin PH, Qian ZY, Liu SB, et al., 2024. A single-cell RNA sequencing guided multienzymatic hydrogel design for self-regenerative repair in diabetic mandibular defects. *Adv Mater*, 36(50):e2410962.
https://doi.org/10.1002/adma.202410962

Lin XF, Wang QQ, Gu CH, et al., 2020. Smart nanosacrificial layer on the bone surface prevents osteoporosis through acid-base neutralization regulated biocascade effects. *J Am Chem Soc*, 142(41):17543-17556.
https://doi.org/10.1021/jacs.0c07309

Liu J, Bao XG, Huang J, et al., 2024. TMEM135 maintains the equilibrium of osteogenesis and adipogenesis by regulating mitochondrial dynamics. *Metabolism*, 152:155767.
https://doi.org/10.1016/j.metabol.2023.155767

Liu XF, Liao YT, Shao JH, et al., 2024. Angelicin improves osteoporosis in ovariectomized rats by reducing ROS production in osteoclasts through regulation of the KAT6A/Nrf2 signalling pathway. *Chin Med*, 19:91.
https://doi.org/10.1186/s13020-024-00961-7

Manolagas SC, 2010. From estrogen-centric to aging and oxidative stress: a revised perspective of the pathogenesis of osteoporosis. *Endocr Rev*, 31(3):266-300.
https://doi.org/10.1210/er.2009-0024

Maqsood M, Suntharalingham S, Khan M, et al., 2024. Complement-mediated two-step NETosis: serum-induced complement activation and calcium influx generate NADPH oxidase-dependent NETs in serum-free conditions. *Int J Mol Sci*, 25(17):9625.
https://doi.org/10.3390/ijms25179625

Morgenstern C, Lastres-Becker I, Demirdöğen BC, et al., 2024. Biomarkers of NRF2 signalling: current status and future challenges. *Redox Biol*, 72:103134.
https://doi.org/10.1016/j.redox.2024.103134

Morris G, Gevezova M, Sarafian V, et al., 2022. Redox regulation of the immune response. *Cell Mol Immunol*, 19(10):1079-1101.
https://doi.org/10.1038/s41423-022-00902-0

Nagaraju G, Udayabhanu, Shivaraj, et al., 2017. Electrochemical heavy metal detection, photocatalytic, photoluminescence, biodiesel production and antibacterial activities of Ag–ZnO nanomaterial. *Mater Res Bull*, 94:54-63.
https://doi.org/10.1016/j.materresbull.2017.05.043

Perera KDC, Weragoda GK, Haputhanthri R, et al., 2021. Study of concentration dependent curcumin interaction with serum biomolecules using ATR-FTIR spectroscopy combined with principal component analysis (PCA) and partial least square regression (PLS-R). *Vib Spectrosc*, 116:103288.
https://doi.org/10.1016/j.vibspec.2021.103288

Qiu X, Liu Y, Shen H, et al., 2021. Single-cell RNA sequencing of human femoral head *in vivo*. *Aging (Albany NY)*, 13(11):15595-15619.
https://doi.org/10.18632/aging.203124

Sheng N, Xing F, Wang J, et al., 2023. Recent progress in bone-repair strategies in diabetic conditions. *Mater Today Bio*, 23:100835.
https://doi.org/10.1016/j.mtbio.2023.100835

Shin JW, Chun KS, Kim DH, et al., 2020. Curcumin induces stabilization of Nrf2 protein through Keap1 cysteine modification. *Biochem Pharmacol*, 173:113820.
https://doi.org/10.1016/j.bcp.2020.113820

Su N, Villicana C, Yang F, 2022. Immunomodulatory strategies for bone regeneration: a review from the perspective of disease types. *Biomaterials*, 286:121604.
https://doi.org/10.1016/j.biomaterials.2022.121604

Sun X, Zhang X, Jiao X, et al., 2022. Injectable bioactive polymethyl methacrylate–hydrogel hybrid bone cement loaded with BMP-2 to improve osteogenesis for percutaneous vertebroplasty and kyphoplasty. *Bio-Des Manuf*, 5:318-332.
https://doi.org/10.1007/s42242-021-00172-1

Tan LP, Cao ZY, Chen H, et al., 2021. Curcumin reduces apoptosis and promotes osteogenesis of human periodontal ligament stem cells under oxidative stress in vitro and in vivo. *Life Sci*, 270:119125.
https://doi.org/10.1016/j.lfs.2021.119125

Tang H, Yu YM, Zhan XX, et al., 2025. Zinc-cobalt bimetallic organic frameworks with antioxidative and osteogenic activities for periodontitis treatment. *Small*, 21(25):2412065.
https://doi.org/10.1002/smll.202412065

Teimouri M, Mirzaee M, Nemati A, et al., 2024. Polysilsesquioxane decorated ZIF-8 as a potential pH-responsive vehicle for topical delivery and release of acyclovir and tetracycline: investigation of blood compatibility, cytotoxicity and antibacterial properties. *Int J Biol Macromol*, 271(Pt 1):132542.
https://doi.org/10.1016/j.ijbiomac.2024.132542

Tomić SL, Babić Radić MM, Vuković JS, et al., 2023. Alginate-based hydrogels and scaffolds for biomedical applications. *Mar Drugs*, 21(3):177.
https://doi.org/10.3390/md21030177

Tsukasaki M, Takayanagi H, 2019. Osteoimmunology: evolving concepts in bone-immune interactions in health and disease. *Nat Rev Immunol*, 19:626-642.
https://doi.org/10.1038/s41577-019-0178-8

Wang JJ, Xie XY, Li H, et al., 2024. Vascular endothelial cells-derived exosomes synergize with curcumin to prevent osteoporosis development. *iScience*, 27(4):109608.
https://doi.org/10.1016/j.isci.2024.109608

Wang LF, Liang YJ, Zhou XH, et al., 2023. Nrf2 differentially regulates osteoclast and osteoblast differentiation for bone homeostasis. *Biochem Biophys Res Commun*, 674:19-26.
https://doi.org/10.1016/j.bbrc.2023.06.080

Wang Y, Sun L, Dong ZL, et al., 2025. Targeted inhibition of ferroptosis in bone marrow mesenchymal stem cells by engineered exosomes alleviates bone loss in smoking-related osteoporosis. *Mater Today Bio*, 31:101501.
https://doi.org/10.1016/j.mtbio.2025.101501

Wang Z, Wang X, Huang Y, et al., 2024. $Ca_v3.3$-mediated endochondral ossification in a three-dimensional bioprinted GelMA hydrogel. *Bio-Des Manuf*, 7:983-999. https://doi.org/10.1007/s42242-024-00287-1

Wu WB, Xiao ZX, Chen Y, et al., 2020. CD39 produced from human GMSCs regulates the balance of osteoclasts and osteoblasts through the Wnt/β-catenin pathway in osteoporosis. *Mol Ther*, 28(6):1518-1532. https://doi.org/10.1016/j.ymthe.2020.04.003

Yan XJ, Zhao XY, Fan MD, et al., 2024. Acidic environment-responsive metal organic framework-mediated dihydroartemisinin delivery for triggering production of reactive oxygen species in drug-resistant lung cancer. *Int J Nanomedicine*, 19:3847-3859. https://doi.org/10.2147/ijn.S451042

Yang XM, Yang XW, Luo P, et al., 2023. Novel one-pot strategy for fabrication of a pH-responsive bone-targeted drug self-frame delivery system for treatment of osteoporosis. *Mater Today Bio*, 20:100688. https://doi.org/10.1016/j.mtbio.2023.100688

Yang Z, Zhang XW, Zhuo FF, et al., 2023. Allosteric activation of transglutaminase 2 via inducing an "open" conformation for osteoblast differentiation. *Adv Sci (Weinh)*, 10(18):2206533. https://doi.org/10.1002/advs.202206533

Yu B, Wang CY, 2016. Osteoporosis: the result of an 'aged' bone microenvironment. *Trends Mol Med*, 22(8):641-644. https://doi.org/10.1016/j.molmed.2016.06.002

Zhang FS, Wu XT, Li QC, et al., 2024. Dual growth factor methacrylic alginate microgels combined with chitosan-based conduits facilitate peripheral nerve repair. *Int J Biol Macromol*, 268(Pt 1):131594. https://doi.org/10.1016/j.ijbiomac.2024.131594

Zhang JY, Zhang RS, Jin SJ, et al., 2024. Curcumin, a plant polyphenol with multiple physiological functions of improving antioxidation, anti-inflammation, immunomodulation and its application in poultry production. *J Anim Physiol Anim Nutr (Berl)*, 108(6):1890-1905. https://doi.org/10.1111/jpn.14029

Zhang W, Zhou XZ, Hou WD, et al., 2023. Reversing the imbalance in bone homeostasis via sustained release of SIRT-1 agonist to promote bone healing under osteoporotic condition. *Bioact Mater*, 19:429-443. https://doi.org/10.1016/j.bioactmat.2022.04.017

Zhang X, Chen JY, Pei X, et al., 2024. Drug-loading ZIF-8 for modification of microporous bone scaffold to promote vascularized bone regeneration. *Chin Chem Lett*, 35(6):108889. https://doi.org/10.1016/j.cclet.2023.108889

Zhao CQ, Shu CQ, Yu JM, et al., 2023. Metal-organic frameworks functionalized biomaterials for promoting bone repair. *Mater Today Bio*, 21:100717. https://doi.org/10.1016/j.mtbio.2023.100717

Zou DB, Mou ZY, Wu WL, et al., 2021. TRIM33 protects osteoblasts from oxidative stress-induced apoptosis in osteoporosis by inhibiting FOXO3a ubiquitylation and degradation. *Aging Cell*, 20(7):e13367. https://doi.org/10.1111/acel.13367

Supplementary information

Figs. S1–S5